ChemComm

ROYAL SOCIETY OF CHEMISTRY

COMMUNICATION

View Article Online
View Journal

Cite this: DOI: 10.1039/d6cc01158f

Received 24th February 2026,
Accepted 15th April 2026

DOI: 10.1039/d6cc01158f

rsc.li/chemcomm

In situ monitoring of a metal recovery process using dual imaging and diffraction

Susanna S. M. Vance,[a] Rebecca Rae,[a] Luke M. M. Kinsman,[a] Caroline Kirk,[a] Liam Perera,[b] Carole A. Morrison *[a] and Jason B. Love *[a]

Continuous technological advancement and depleting natural sources of key metals such as gold necessitate highly selective recovery processes from secondary sources. Herein, we report the visualisation of a recyclable precipitation process using dual imaging and diffraction that gives insight into the mechanism of precipitation and highlights the possibility of kinetic separations.

For centuries, gold has been regarded as an important and valuable metal, finding historical use in jewellery and currency, while modern applications, particularly in the electronics sector, span many industries.[1,2] As a result, natural sources of gold are diminishing, necessitating suitable alternative sources that satisfy both economic and environmental stipulations.[3] Waste electronic and electrical equipment (WEEE or e-waste) is a secondary source of gold with concentrations often exceeding those in mineral ores.[4] However, the variable and complex composition of e-waste can make separation challenging,[5] necessitating the need for highly selective and efficient recovery processes to capitalise on this valuable waste stream.[6] Precipitation methods using recyclable reagents are garnering attention as promising alternatives to solvent extraction techniques for gold recovery, as they negate the use of toxic organic solvents that present safety and environmental concerns when used on an industrial scale. Selectivity for gold can be achieved using reagents that exploit molecular recognition,[7–11] reduction within metal- and covalent-organic frameworks (MOFs and COFs),[12,13] and through size discrimination in porous porphyrin polymers.[14–17] Selective gold recovery has also been reported for sorbents,[18] adsorbents[19,20] and magnetic nanoparticles.[21] We previously reported that the simple diamide **L** (see Scheme 1) acts as a recyclable reagent for the highly selective precipitation of gold from acidic mixed–metal solutions typical of e-waste leach streams.[22] Tuning the acid concentration caused the precipitation of other metals such as iron, gallium and tin with the preferential selectivity for gold rationalised on thermodynamic grounds.[23] The precipitation was thought to occur through a dissolution–precipitation mechanism,[22] with qualitative kinetic analysis suggesting a faster timescale for gold recovery compared with other metals. In this work, we directly visualise and interrogate the *in situ* nucleation and crystal growth mechanisms for the precipitation of gold and iron upon complexation with **L** and establish if kinetic separation is possible by this system. Due to set-up challenges, *in situ* precipitation studies are often confined to reaction monitoring *via* a singular technique, such as spectroscopy, imaging or diffraction techniques, and ex-situ experiments.[24–28] In contrast, here we report the use of dual imaging and diffraction, made possible by the capabilities of beamline K11 at the Diamond Light Source. In addition, a bespoke flow cell was designed for this work that allows for the use of corrosive reagents such as HCl.[29]

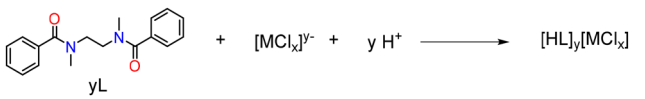

Scheme 1 Reaction scheme for the formation of the precipitated metal complexes of **L**, where M = Au, Fe, Ga or Sn.

In the first instance, dry samples of **L** and the end products for gold, [**HL**][$AuCl_4$] and iron, [**HL**][$FeCl_4$] (10–15 mg), were packed into sample cells (see Fig. S1) and diffraction patterns and tomography scans for each were recorded for comparison with the *in situ* phases formed. Flow samples were prepared by adding solid **L** (10–15 mg) to the sample cell (see SI Fig. S1) followed by a drop of aqueous solution prior to attachment of the fluid cartridge and subsequent liquid flow. This step minimised movement of the sample when flow was initiated, which improved the quality of the tomography scans and facilitated more straightforward reconstruction of the images obtained.

Typically, an initial tomography scan and diffraction pattern were recorded before flow of the acidic metal solution was started, with a flow rate of 10 μL min^{-1} used for all samples.

[a] School of Chemistry, University of Edinburgh, Joseph Black Building, Kings Buildings, EH9 3FJ, UK. E-mail: c.morrison@ed.ac.uk
[b] Diamond Light Source, Harwell Science and Innovation Campus, Didcot, Oxfordshire, OX11 0DE, UK

Due to set-up limitations (specifically, the position of the imaging camera, along with the relatively small beam size and large sample thickness), some of the high intensity, low angle peaks are missing from all PXRD patterns, and therefore refinement of these data could not be undertaken. However, for the purposes of this study, phase identification is sufficient to inform on the composition, as full characterisation of **L** and metal complexes was carried out in our previous work.[22,23]

Visualisation of the precipitation of iron by **L** was investigated first, as prior experiments suggested this reaction is slower than for gold, thereby allowing for more facile capture of *in situ* changes. Solid **L** was added to the sample cell followed by a drop of the metal solution (0.005 M $FeCl_3$ in 6 M HCl). An initial tomography image and diffraction pattern were recorded (T = 0 min), followed by a second tomography scan and diffraction pattern to ensure the sample was static. The metal solution (also 0.005 M $FeCl_3$ in 6 M HCl) from the fluid cartridge was pulled through the sample for 10 min at a flow rate of 10 μL min^{-1} and allowed to stand for 10 min to reduce sample movement prior to tomography and diffraction data being recorded. At T = 0, the diffraction pattern agrees with that of **L** (Fig. 1(a)). The pattern remains essentially unchanged for the first 65 min of metal-fluid flow, with no discernible peaks seen for the expected complex, [H**L**][$FeCl_4$]. The peak intensities decrease over this time, however, which likely results from the dissolution of **L**. Low intensity peaks (Q = 1.18 $Å^{-1}$ and Q = 1.37 $Å^{-1}$) begin to appear after T = 125 min, which do not match those expected for either **L** or the end-product phase, [H**L**][$FeCl_4$]. These peaks continue to grow, becoming the major phase at T = 245 min. As the final pattern does not correspond

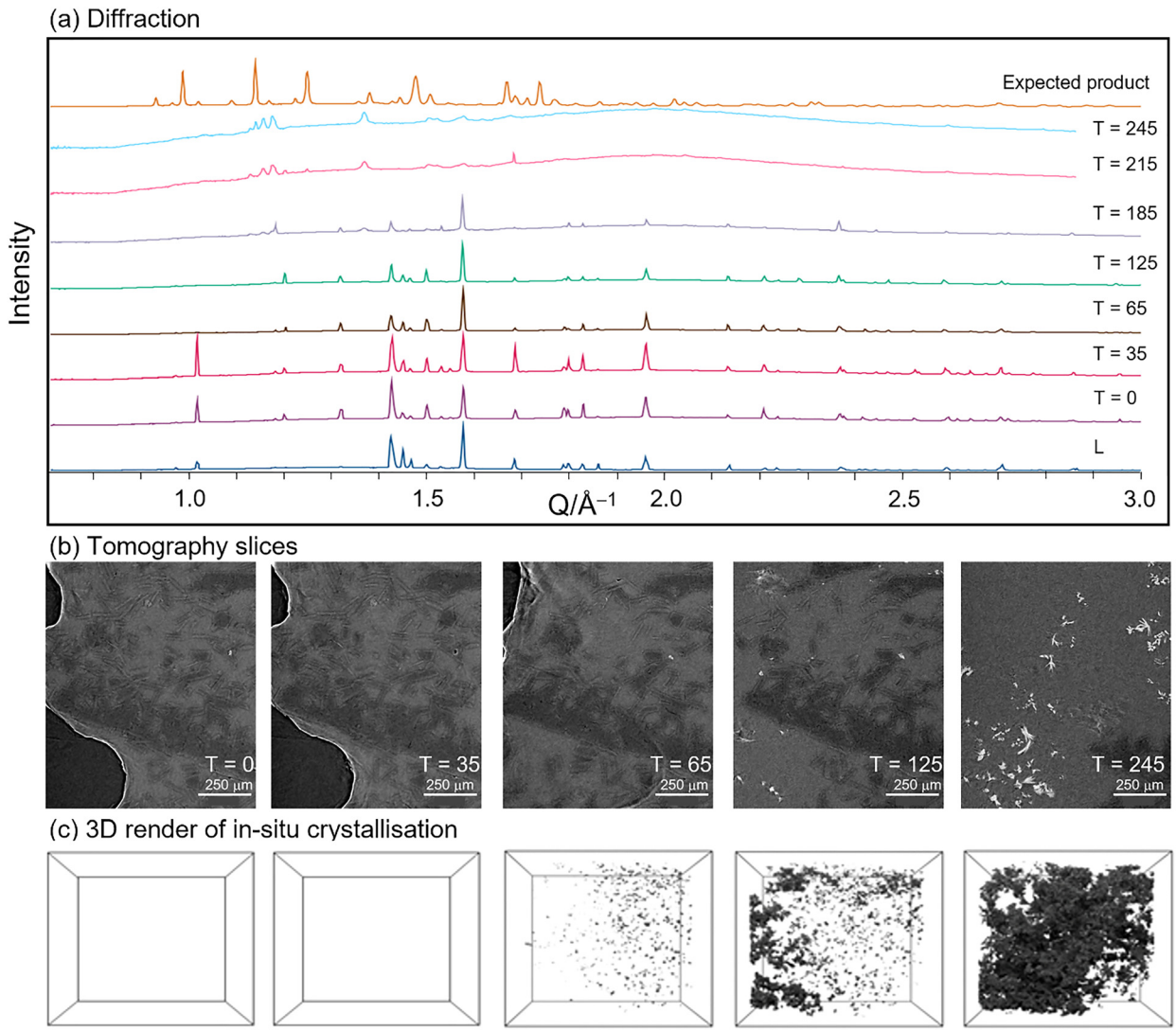

Fig. 1 (a) Sequential summed diffraction patterns from vertical line scan at selected timepoints (T) in minutes showing the formation of precipitated [H**L**][$FeCl_4$]. Diffraction patterns for **L** and the expected end-product are also shown for reference. PXRD patterns have been normalised for clarity; (b) Sequential X/Z slices at selected timepoints for the precipitation of an iron-containing complex. Dark features represent the initial material **L** and light regions correspond to [H**L**][$FeCl_4$], and (c) Sequential three-dimensional renders of the reconstructed sample cell volume showing the growth of the [H**L**][$FeCl_4$] phase (scale 1 × 1 × 1 mm of region of interest from the tomography scans).

to the expected product it is likely that this represents a previously unseen polymorph of [HL][$FeCl_4$] or a different reaction product. Note the high baseline in the T = 215 and 245 min patterns can be attributed to poor diffraction from the small crystals suspended in solution. In the sequential X/Z slices taken from the reconstructed volume of the tomography scans (Fig. 1(b), **L** is initially seen as dark block-like features with defined edges that are partially obscured in the early images due to the presence of the metal solution. These are more apparent in the lighter areas of the tomography images, and have considerably reduced in number by T = 245 min. At T = 65 min, some contrast in the image becomes apparent as nucleation begins, with the light regions attributed to formation of the metal complex. This is further evidenced by the observed growth of dendritic-like crystals in the three-dimensional (3D) render at T = 65 min, which shows that small crystals have formed throughout the entire volume of the sample cell (Fig. 1(c)). Nucleation occurs on the edges of crystals of **L** and, as the reaction progresses, the disappearance of the dark block-like features and the appearance of bright of small plate-like dendritic crystals (Fig. 1(b)), supporting a dissolution–precipitation mechanism. The majority of **L** is dissolved after T = 245 min, with the 3D render showing that the precipitated metal complex now occupies most of the sample cell volume (Fig. 1(c)). These images correlate well with the diffraction data, with minimal change in the composition of the solid observed at T = 65 min, and formation of a complex observed from T = 125 min onwards. While it would be highly desirable to segment the tomography scans, to further quantify the transition from **L** to the precipitate, the quality of the greyscale images collected in this study was not sufficiently high to perform this analysis reliably. Moreover, as the reaction proceeds *via* a dissolution–precipitation process, some of **L** will likely be washed out of the reaction vessel by the metal-containing solution, further impeding the accuracy of any quantitative analysis. However, in principle, an improved data

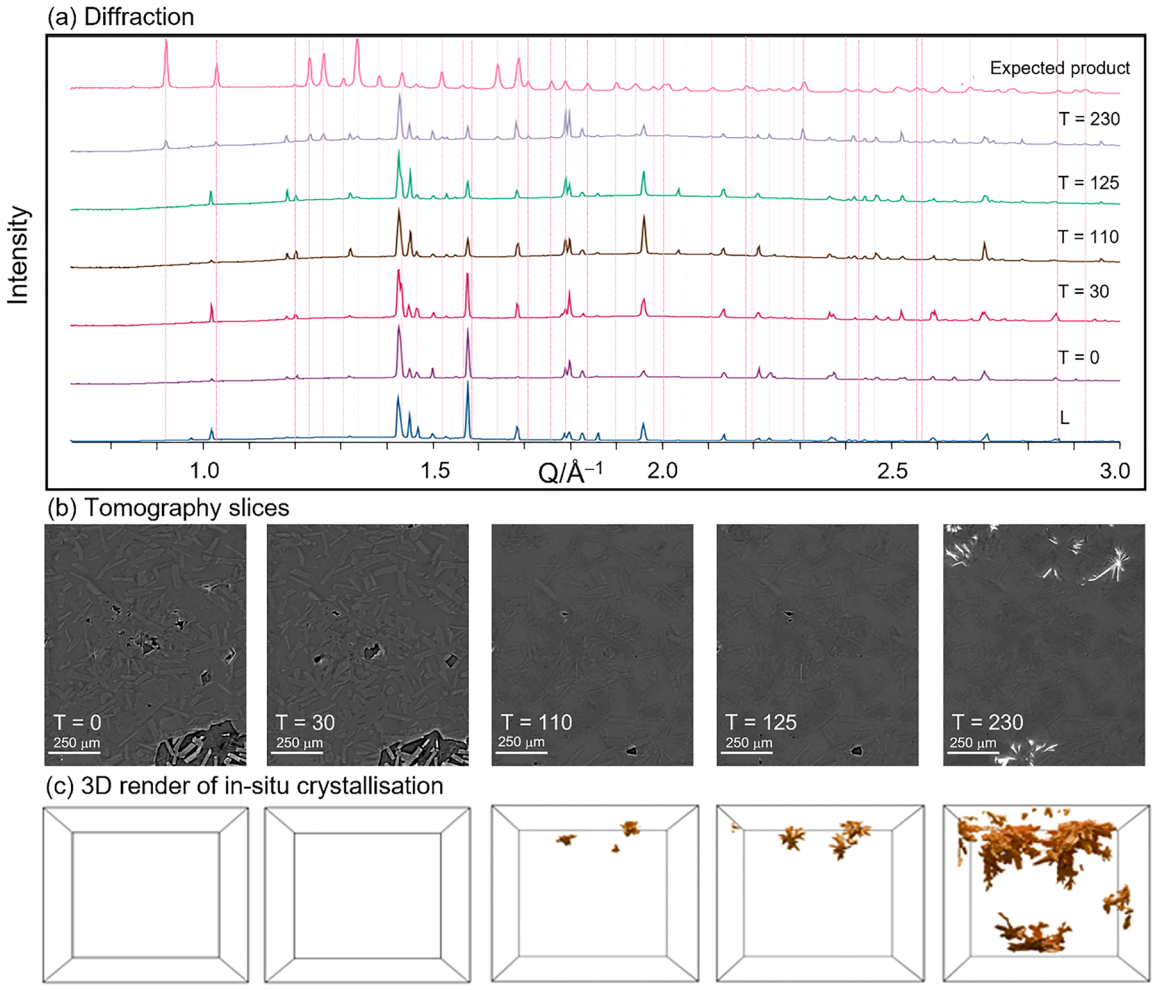

Fig. 2 (a) Sequential summed diffraction patterns from vertical line scan at selected timepoints (T) in minutes showing the formation of precipitated [H**L**][$AuCl_4$]. Diffraction patterns for **L** and the expected end-product (pink dotted lines) are also shown for reference. PXRD patterns have been normalised for clarity; (b) Sequential X/Z slices at selected timepoints for the precipitation of a gold-containing complex. Dark features represent the initial **L** phase and light regions correspond to [H**L**][$AuCl_4$]; and (c) Sequential three-dimensional renders of the reconstructed sample cell volume showing the growth of the [H**L**][$AuCl_4$] phase (scale 1 × 1 × 1 mm of region of interest from the tomography scans).

collection strategy that boosted data resolution could present an insightful way to monitor the kinetics of the precipitation reaction.

With the mechanism established for iron uptake by **L**, the process was repeated for gold. Solid **L** (10–15 mg) was added to a sample cell with a drop of the metal solution (0.005 M $HAuCl_4$ in 6 M HCl). In this case, however, the initial tomography and diffraction pattern suggest that the reaction had gone to completion, indicating a much more rapid timescale for this reaction (Fig. S2 and S3). Therefore, in a second run, the metal solution was diluted (to 0.003 M $AuCl_4$) and the acid concentration decreased (to 4 M) to slow the reaction to a timescale that could be more easily monitored. In addition, the fluid flow was reduced to 5 min with a wait time of 2 min, and a drop of ultra-pure H_2O added to the solid sample **L** instead of the metal solution to prevent reaction before flow; this set-up proved successful. From T = 0–110 min, the phases agree with that of **L** (Fig. 2(a); thereafter the first peak commensurate with the expected pattern for the end-product [H**L**][$AuCl_4$] is observed (at Q = 1.34 Å^{-1}), with further peaks observed by T = 230 min.

At T = 230 min, the major phase present matches the expected product structure by phase ID (according to peak placement, we note the likely effects of preferred orientation affecting peak intensities). As with the iron study, these diffraction data correlate well with the tomography, in which **L** appears as dark block-like features (Fig. 2(b)), which are more discernible in this case, likely due to the reduced concentration of the gold solution compared with iron. The precipitated metal complex again presents as bright dendritic crystals, which are readily visible in the 3D render (Fig. 2(c)) and are first observed at T = 110 min. Nucleation and subsequent crystal growth occur similarly at the edges of crystals of **L** in regions where significant dissolution of **L** has occurred, further supporting a dissolution–precipitation mechanism. At T = 230 min large dendritic crystals encompass a significant portion of the sample cell volume. While the reaction time following nucleation is similar for both systems (iron = 180 min and gold = 120 min) the metal and acid concentrations were significantly reduced for the gold study. This is compelling evidence that the precipitation kinetics are likely significantly faster for [H**L**][$AuCl_4$] than for [H**L**][$FeCl_4$]. Taken with our previous work that established that [H**L**][$AuCl_4$] was the thermodynamic product,[23] these new data suggest that this complex is also the kinetic product. This study, to our knowledge, presents the first *in situ* analyses of a metal recovery system in flow using dual imaging and diffraction, made possible by the unique set-up at beamline K11 at the Diamond Light Source.

S.S.M.V carried out all synthetic experimental work. S.S.M.V, R.R., C.A.M. and L.P. prepared samples for analysis and collected the data at the Diamond Light Source. S.S.M.V, R.R., L.M.M.K, C.K., L.P., C.A.M. and J.B.L. analysed the data and wrote the manuscript. C.A.M. and J.B.L. directed the research.

Conflicts of interest

There are no conflicts to declare.

Data availability

The PXRD data are available in the Edinburgh Datashare repository (https://doi.org/10.7488/ds/8080). The authors declare all additional data that relate to the findings of this study are available within the paper or in the supplementary information (SI). Supplementary information is available. See DOI: https://doi.org/10.1039/d6cc01158f.

References

1 C. W. Corti and R. J. Holliday, *Gold Bull.*, 2004, **37**, 20–26.
2 S. Althaf and C. W. Babbitt, *Resour., Conserv. Recycl.*, 2021, **167**, 105248.
3 R. M. Izatt, S. R. Izatt, R. L. Bruening, N. E. Izatt and B. A. Moyer, *Chem. Soc. Rev.*, 2014, **43**, 2451–2475.
4 C. Hagelüken and C. W. Corti, *Gold Bull.*, 2010, **43**, 209–220.
5 M. Huy Do, G. Tien Nguyen, U. Dong Thach, Y. Lee and T. Huu Bui, *Miner. Eng.*, 2023, **191**, 107977.
6 M. Kaya, *Waste Manage.*, 2016, **57**, 64–90.
7 S. S. Braga, *Beilstein J. Org. Chem.*, 2025, **21**, 1116–1125.
8 L. X. Chen, M. Liu, Y. Q. Zhang, Q. J. Zhu, J. X. Liu, B. X. Zhu and Z. Tao, *Chem. Commun. (Camb.)*, 2019, **55**, 14271–14274.
9 Z. Liu, M. Frasconi, J. Lei, Z. J. Brown, Z. Zhu, D. Cao, J. Iehl, G. Liu, A. C. Fahrenbach, Y. Y. Botros, O. K. Farha, J. T. Hupp, C. A. Mirkin and J. F. Stoddart, *Nat. Commun.*, 2013, **4**, 1855.
10 A. Nag, M. R. Islam and T. Pradeep, *ACS Sustainable Chem. Eng.*, 2021, **9**, 2129–2135.
11 C. C. Shaffer and B. D. Smith, *Org. Chem. Front.*, 2021, **8**, 1294–1301.
12 M. Mon, J. Ferrando-Soria, T. Grancha, F. R. Fortea-Perez, J. Gascon, A. Leyva-Perez, D. Armentano and E. Pardo, *J. Am. Chem. Soc.*, 2016, **138**, 7864–7867.
13 D. T. Sun, N. Gasilova, S. Yang, E. Oveisi and W. L. Queen, *J. Am. Chem. Soc.*, 2018, **140**, 16697–16703.
14 Y. Hong, D. Thirion, S. Subramanian, M. Yoo, H. Choi, H. Y. Kim, J. F. Stoddart and C. T. Yavuz, *Proc. Natl. Acad. Sci. U. S. A.*, 2020, **117**, 16174–16180.
15 T. S. Nguyen, Y. Hong, N. A. Dogan and C. T. Yavuz, *Chem. Mater.*, 2020, **32**, 5343–5349.
16 Y. Wang, Q. Lu, X. Cui and W. Lu, *ACS Appl. Polym. Mater.*, 2024, **6**, 1449–1459.
17 A. Preetam, A. Modak, S. N. Naik, K. K. Pant and V. Kumar, *ACS Appl. Polym. Mater.*, 2024, **6**, 3676–3689.
18 M. Mann, T. P. Nicholls, H. D. Patel, L. S. Lisboa, J. M. M. Pople, L. N. Pham, M. J. H. Worthington, M. R. Smith, Y. Yin, G. G. Andersson, C. T. Gibson, L. J. Esdaile, C. E. Lenehan, M. L. Coote, Z. Jia and J. M. Chalker, *Nat. Sustainable*, 2025, **8**, 947–956.
19 D. Kang, C. Xing, C. Zhang, S. Wang, Y. Dong, D. Yang and W. Sun, *Nanoscale Horiz.*, 2025, **10**, 2541–2549.
20 X. Zhou, C. Liao, J. Liang, M. Liu, H. Xiao, F. Liu and Y. Zeng, *Sep. Purif. Technol.*, 2025, **362**, 131625.
21 J. Ren, J. Wang, M. Guo, R. Li and Y. Guan, *J. Environ. Manage.*, 2025, **386**, 125793.
22 L. M. M. Kinsman, B. T. Ngwenya, C. A. Morrison and J. B. Love, *Nat. Commun.*, 2021, **12**, 6258.
23 S. S. M. Vance, M. Mojsak, L. M. M. Kinsman, R. Rae, C. Kirk, J. B. Love and C. A. Morrison, *Inorg. Chem.*, 2024, **63**, 9332–9345.
24 O. L. J. Virtanen, M. Kather, J. Meyer-Kirschner, A. Melle, A. Radulescu, J. Viell, A. Mitsos, A. Pich and W. Richtering, *ACS Omega*, 2019, **4**, 3690–3699.
25 Z. Feng, P. Barai, J. Gim, K. Yuan, Y. A. Wu, Y. Xie, Y. Liu and V. Srinivasan, *J. Electrochem. Soc.*, 2018, **165**, A3077.
26 M. Salim, S. J. Fraser-Miller, K. Bērziņš, J. J. Sutton, K. C. Gordon and B. J. Boyd, *Pharmaceutics*, 2023, **15**(7), 1968.
27 J. Li and F. L. Deepak, *Chem. Rev.*, 2022, **122**, 16911–16982.
28 H. Wang, M. Mutailpu, L. Boddapati, A. Samanta, F. L. Deepack and J. Li, *J. Am. Chem. Soc.*, 2025, **147**, 22104–22114.
29 L. Perera, P. Garland, C. Kirk, A. Leonardi, J. B. Love, T. Manchester, C. A. Morrison, R. Rae, S. S. M. Vance and S. I. Ahmed, *J. Synchrotron Radiat.*, 2026, **33**, 511–515.

